PHYSICAL REVIEW E **88**, 042710 (2013)

Optimal mapping of x-ray laser diffraction patterns into three dimensions using routing algorithms

Stephan Kassemeyer,[1,2] Aliakbar Jafarpour,[1,2] Lukas Lomb,[1,2] Jan Steinbrener,[1,2] Andrew V. Martin,[3] and Ilme Schlichting[1,2]
[1]*Max-Planck-Institut für medizinische Forschung, Jahnstr. 29, 69120 Heidelberg*
[2]*Max Planck Advanced Study Group, Center for Free-Electron Laser Science (CFEL), Notkestr. 85, 22607 Hamburg, Germany*
[3]*ARC Centre of Excellence for Coherent X-ray Science, School of Physics, The University of Melbourne, Victoria 3010, Australia*
(Received 1 November 2012; revised manuscript received 3 October 2013; published 28 October 2013)

Coherent diffractive imaging with x-ray free-electron lasers (XFEL) promises high-resolution structure determination of noncrystalline objects. Randomly oriented particles are exposed to XFEL pulses for acquisition of two-dimensional (2D) diffraction snapshots. The knowledge of their orientations enables 3D imaging by multiview reconstruction, combining 2D diffraction snapshots in different orientations. Here we introduce a globally optimal algorithm that can infer these orientations. We apply it to experimental XFEL data of nanoparticles and so determine their 3D electron density.

DOI: 10.1103/PhysRevE.88.042710 PACS number(s): 87.59.−e, 41.60.Cr, 42.30.−d, 42.55.Vc

I. INTRODUCTION

Since femtosecond x-ray pulses can pass through a microscopic sample before the onset of significant radiation damage, one of the most promising scientific applications of x-ray free-electron lasers (XFELs) is in subnanometer resolution imaging of biological objects, including cells, viruses, macromolecular assemblies, and nanocrystals. This concept of "diffraction-before-destruction" [1,2] has been validated recently at the Linac Coherent Light Source (LCLS) for protein micro- and nanocrystals [3–5], single mimi viruses [6], and airborne particulate matter [7], demonstrating high-resolution protein structure analysis [4] and two-dimensional (2D) projection imaging [6–9]. A full three-dimensional (3D) structure analysis requires the 3D diffraction volume to be sampled by 2D diffraction patterns in different object orientations. Since the extremely bright FEL x-ray pulses completely destroy the sample objects, a stream of identical sample particles is injected and the different diffraction images are collected serially. Experimentally, it is extremely challenging to either set or determine the orientation of the particles prior to their interaction with the x-ray beam. Instead, the particles are injected in unknown, random orientations and postexperiment extraction of the object orientation becomes a critical step in the structure determination process. Once the orientational relationships of the 2D diffraction patterns (and thus the orientations of the different sample particles) are known, it is straightforward to assemble the 2D diffraction patterns into a 3D diffraction volume enabling a 3D reconstruction. Algorithms for establishing particle orientations must cope with practical obstacles, including extremely low diffraction signals, constraints imposed by particle symmetry, the possible presence of numerous particle conformations, and otherwise inhomogeneous data sets. To date the success in developing such algorithms has been limited.

Here we present a new approach based on pairwise comparisons of the measured diffraction patterns. The underlying principle is that objects of incrementally different orientation will yield diffraction patterns that differ only incrementally. Given a large enough number of measured diffraction patterns, it becomes possible—via pairwise comparisons—to arrange the entire ensemble of measured diffraction patterns in what might be called similarity sequences. For a rigid object rotating about its center of mass, the most direct transition between two separate object orientations is a rotation about a specific single rotation axis. The similarity sequences allow this specific axis to be identified and thereby the angular relationships between the 2D diffraction patterns can be established.

II. ESTABLISHING AND INTERPRETING SIMILARITIES AMONG DIFFRACTION PATTERNS

When the FEL x-ray beam scatters forwards from a randomly oriented 3D object and onto a detector centered on the x-ray beam axis, the resulting diffraction pattern corresponds to a (spherical) slice through the object in reciprocal space. Due to the properties of the underlying Fourier transform, the mapping from the space of object orientations to the space of diffraction patterns is continuous, i.e., a slight rotation of the object induces only a correspondingly slight change in the diffraction pattern. Consequently, a measure $d_{\text{diss}}(P_1,P_2)$ of the "dissimilarity" between two different diffraction patterns P_1,P_2 provides a local measure of the angular separation between the two corresponding objects. Here we use the Pearson correlation coefficient to estimate the dissimilarity d_{diss}. In order to extend this local estimate of angular distances (slight changes in diffraction patterns corresponding to slight object rotations) to global quantities (arbitrary changes in diffraction patterns corresponding to possibly large rotations), we define the "geodesic dissimilarity" d_{geo} between two patterns P_1 and P_2 to be the shortest accumulated dissimilarity of all possible sequences $\{\gamma_k\}$ of diffraction patterns starting from P_1 and ending at P_2,

$$d_{\text{geo}}(P_1,P_2) = \min_{\gamma\in\Gamma(P_1,P_2)} \sum_{i=0}^{|\gamma|-1} d_{\text{diss}}(\gamma_i,\gamma_{i+1}).$$

To cope with the local nature of d_{diss}, the optimization is limited to a subset Γ of sequences with similar consecutive elements based on a threshold ε: $\Gamma(P_1,P_2) = \{\{\gamma_k\}_{k=0}^{N} \mid (\gamma_0 = P_1) \wedge (\gamma_N = P_2) \wedge (d_{\text{diss}}(\gamma_i,\gamma_{i+1}) < \varepsilon \forall i = 1\ldots N-1)\}$. We name the optimal sequence $\gamma(P_1,P_2)$ of this subset the *geodesic sequence* or *shortest path* between P_1 and P_2.

The search for the shortest path on the discrete graph of diffraction patterns has an analogy to the rotation group SO(3): A geodesic on SO(3) with respect to the angular distance $d_\angle$ is a rotation about a single axis (generally called the Euler axis). It is useful to likewise associate the shortest similarity path between two diffraction patterns with a "geodesic" trajectory that can be interpreted as a rotation about an Euler axis. This correspondence only holds if the true angular distance $d_\angle$ is used which is unknown in general. Since d_{diss} locally (for small angles) correlates with $d_\angle$ we use it to approximate $d_\angle$. To justify this approximation we have carried out a number of numerical simulations and, on that basis, convinced ourselves that quite generally the "shortest" similarity sequence that smoothly connects two diffraction patterns (i.e., the path through diffraction-pattern space having minimal cumulative dissimilarity) corresponds to the smallest real space rotation of the object.

This mapping of similarity geodesics onto real space geodesics must be very carefully considered. In general, the distance measure defined by the dissimilarity can be distorted by any anisotropies of the experimental geometry or of the object itself and thus deviate from the round metric of S^3. One obvious anisotropy, as pointed out in Ref. [10], is that due to the unidirectional nature of the x-ray beam which, as a first approximation, results in a projection. However, this distortion is easily treated by simply distinguishing rotations about the x-ray beam axis (which we term "in-plane rotations") from rotations about axes orthogonal to the x-ray beam axis ("out-of-plane rotations," see below). The consequences of anisotropies in object shape are difficult to characterize in a general fashion. However, in simulations with parameters typical for coherent diffraction imaging experiments and reasonable sample object shapes (finite size and thickness), we find the effect of distortions due to object shape to be negligible. As shown in Fig. 1, even under severe distortion the geodesics do not deviate much from great circles on S^3 and thus they correspond to single axis rotations. Accordingly, we consider this mapping of similarity geodesics (within diffraction patterns) onto real space geodesics (of object orientation) to be generally valid and can refer to either as simply a "geodesic."

The topological information on geodesic sequences can be translated into geometric information on the orientations by comparison with distinct angles such as the maximum geodesic angle. Provided that the number of diffraction patterns is sufficient to approximate a complete sampling of the orientation space, the longest geodesic sequence found

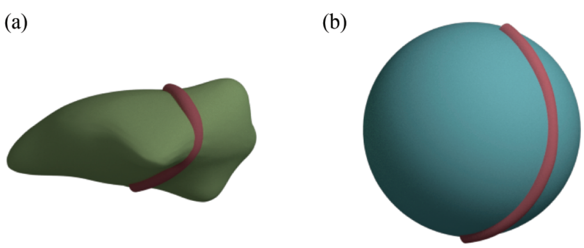

FIG. 1. (Color online) Illustration of the effect of distortions on geodesics. The similarity metric of diffraction snapshots can be distorted, deviating from the round metric induced by S^3. (a) shows a 3D slice through the heavily distorted three-sphere S^3 and a geodesic line (red). Mapping back to S^3 (b) shows that even under heavy distortion the geodesic is approximately preserved, i.e., it is a great circle on S^3.

in the data corresponds to the maximum geodesic angular separation, which depends on the sample symmetry (180° for asymmetric objects). The object symmetry can be assessed from the diffraction patterns, assisted by the observation that the geodesic sequences end on symmetry poles, since beyond those the diffraction patterns increasingly resemble the starting diffraction pattern.

III. IDENTIFYING IN-PLANE AND OUT-OF-PLANE ROTATIONS AND COMBINING THEM TO SPAN THE ORIENTATION SPACE

Two steps are required to successfully recover the orientations of all collected diffraction patterns of given sample objects via geodesic analysis: First, each pattern has to be assigned to a geodesic sequence and then the relations between their respective Euler axes need to be established. The former involves an optimization that can be carried out efficiently by dynamic programming algorithms like Dijkstra's shortest path algorithm [11] while the latter can be realized by adding another source of angular information with the aid of "in-plane" rotations. Typical setups for diffraction experiments are symmetric with respect to the x-ray beam axis. Due to this symmetry, rotating the specimen about the x-ray beam axis corresponds to a rotation of the diffraction pattern in the detector plane by that same angle (Fig. 2). Starting from a diffraction pattern P we can therefore identify or generate a "synthetic" diffraction pattern $P(\alpha)$ that is rotated in-plane through an angle α. Given two diffraction patterns P_1 and P_2 whose orientations are related by the Euler axis $\vec{E}_{0,0}$, introducing synthetic in-plane rotations $P_1 \rightarrow P_1(\alpha)$ and $P_2 \rightarrow P_2(\beta)$ will lead to the Euler axis $\vec{E}_{\alpha,\beta}$ of a geodesic sequence $\gamma(P_1(\alpha), P_2(\beta))$. The fraction of diffraction patterns that can be assigned to such sequences depends on the angular separation θ and on the orientation of the Euler axis $\vec{E}_{0,0}$ relative to the x-ray axis $\vec{c}$ (the in-plane axis). The second dependance can be understood as follows: in-plane rotations are also geodesic rotations and in the extreme case where $\vec{E}_{0,0} = \vec{c}$, there is no difference between in-plane rotations and the geodesic rotation that rotates P_1 to P_2 and thus the in-plane rotations do not provide additional information. To maximize the information gain that can be obtained from in-plane rotations we have to minimize the overlap between in-plane rotations and the geodesic rotation by choosing P_2 such that the geodesic rotation that rotates P_1 to P_2 is orthogonal to the in-plane rotations. We name these orthogonal rotations "out-of-plane" rotations from now on. This suggests that the maximum number of diffraction patterns can be assigned to geodesic sequences $\gamma(P_1(\alpha), P_2(\beta))$ if P_1 and P_2 are separated by the maximum geodesic angle $\theta = 180°$ and if the corresponding Euler axis $\vec{E}_{0,0}$ is orthogonal to the x-ray axis $\vec{c}$. In fact, as shown in Appendix A and illustrated in Figs. 2(b) and 2(c), this covers all diffraction patterns and all orientations. In-plane and out-of-plane rotations can be orthogonalized by artificially setting $d_{\text{diss}}(P_1, P_1(\alpha))$ to zero for all values of α. Then, initial in-plane rotations will be preferred in the search for the shortest path because they are cost-free. In this way, the in-plane component is only contained in the selection step between P_1 and the next diffraction pattern in

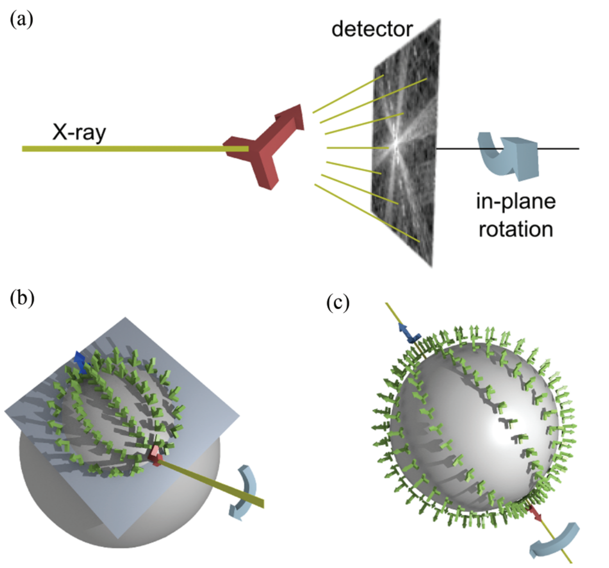

FIG. 2. (Color online) Illustration of the geodesic and in-plane rotations algorithm (GIPRAL). (a) Geometry of diffraction experiment. The triad (red) denotes the object and its orientation. In-plane rotations correspond to a rotation of both object and diffraction pattern around the x-ray axis. [(b) and (c)] Illustration of combined geodesic and in-plane rotations. For clarity, only the dark gray (red) object $O(P_1)$ corresponding to diffraction pattern P_1 is rotated in-plane around the x-ray beam [light gray (yellow line)]. The geodesic sequences connecting the orientations of each in-plane rotation of $O(P_1)$ [dark gray (red)] to $O(P_2)$ [dark gray (blue)] are shown in light gray (green). (b) In-plane rotations of $O(P_1)$ with arbitrary orientation (see www.gipral.org for an interactive illustration). (c) Maximum separation between the object orientations $O(P_1)$ and $O(P_2)$ leads to full coverage of SO(3). The orientations of the red and the blue arrows constitute the poles on S^3. Note that only its projection S^2 can be shown here.

the geodesic sequence and can easily be removed, leading to out-of-plane geodesic sequences which are orthogonal to the in-plane rotations.

In order to calculate the effect of combining in-plane and out-of-plane rotations, consider a diffraction pattern $P_{\alpha,\beta,\varphi}$ which is part of the geodesic sequence $\gamma(P_1(\alpha), P_2(\beta))$ with the geodesic angle φ (see Fig. 3). Here we derive the orientation of $P_{\alpha,\beta,\varphi}$ relative to the orientation of P_1 under the condition that P_2 is related to P_1 by a true out-of-plane rotation (without in-plane components) through the angle θ. The coordinate system is chosen such that the y axis coincides with the rotation axis $\vec{\boldsymbol{a}}$ of the out-of-plane rotations and the z axis coincides with the x-ray axis $\vec{\mathbf{c}}$ (= in-plane axis). We describe orientations as rotations of a reference orientation so they can be expressed in quaternions

$$\boldsymbol{q}_{\vec{e},\vartheta} = \begin{pmatrix} \sin(\vartheta/2)\vec{\boldsymbol{e}} \\ \cos(\vartheta/2) \end{pmatrix},$$

where $(\vec{\boldsymbol{e}},\vartheta)$ is the Euler axis-angle representation. In this orientation representation, the unit quaternion $\boldsymbol{q} = \mathbb{1}$ stands for the reference orientation which, for conveniance, we define as the orientation of the diffraction pattern P_1. Thus the orientation of $P_1(\alpha)$ is the in-plane rotated reference

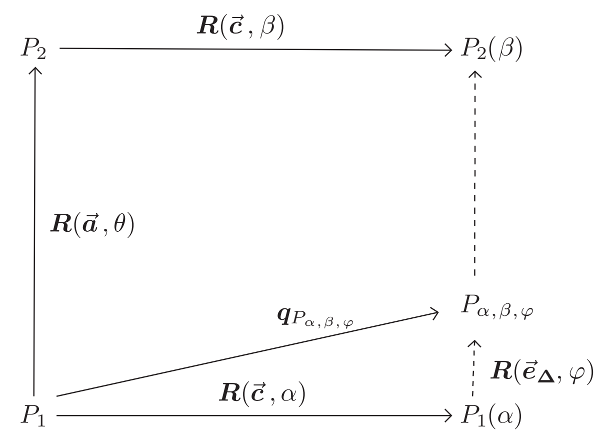

FIG. 3. Relations between diffraction patterns and rotation operators $\boldsymbol{R}$. The Solid vertical arrow describes geodesic out-of-plane operations (rotations about $\vec{\boldsymbol{a}}$), horizontal operators describe in-plane operations (rotations about $\vec{\boldsymbol{c}}$). Note that in the special case $\theta = 180^\circ$ the dashed arrows are out-of-plane rotations, too.

orientation and can be written as

$$\boldsymbol{q}_{P_1(\alpha)} = \begin{pmatrix} 0 \\ 0 \\ \sin(\alpha/2) \\ \cos(\alpha/2) \end{pmatrix}.$$

The orientation of P_2 is related to that of P_1 by an out-of-plane rotation through the angle θ and can be written as

$$\boldsymbol{q}_{P_2} = \begin{pmatrix} 0 \\ \sin(\theta/2) \\ 0 \\ \cos(\theta/2) \end{pmatrix}.$$

The orientation of $P_2(\beta)$ can be obtained by adding an in-plane rotation through the angle β to $\boldsymbol{q}_{P_2}$:

$$\boldsymbol{q}_{P_2(\beta)} = \begin{pmatrix} 0 \\ 0 \\ \sin(\beta/2) \\ \cos(\beta/2) \end{pmatrix} \otimes \boldsymbol{q}_{P_2} = \begin{pmatrix} -\sin(\theta/2)\sin(\beta/2) \\ \sin(\theta/2)\cos(\beta/2) \\ \cos(\theta/2)\sin(\beta/2) \\ \cos(\theta/2)\cos(\beta/2) \end{pmatrix}.$$

The geodesic rotation $\boldsymbol{q}_{\boldsymbol{\Delta}}$ from $P_1(\alpha)$ to $P_2(\beta)$ is given by

$$\boldsymbol{q}_{\boldsymbol{\Delta}} = \boldsymbol{q}_{P_2(\beta)} \otimes \boldsymbol{q}^{-1}_{P_1(\alpha)} = \begin{pmatrix} -\sin(\theta/2)\sin(\beta/2+\alpha/2) \\ \sin(\theta/2)\cos(\beta/2+\alpha/2) \\ \cos(\theta/2)\sin(\beta/2-\alpha/2) \\ \cos(\theta/2)\cos(\beta/2-\alpha/2) \end{pmatrix}.$$

The rotation axis $\vec{\boldsymbol{e}}_{\boldsymbol{\Delta}}$ of all rotations that are part of the geodesic connecting $P_1(\alpha)$ and $P_2(\beta)$ can be extracted from the vector part of $\boldsymbol{q}_\Delta$:

$$\vec{\boldsymbol{e}}_\Delta = \frac{1}{|\vec{\boldsymbol{q}}_\Delta|}\begin{pmatrix} -\sin(\theta/2)\sin(\beta/2+\alpha/2) \\ \sin(\theta/2)\cos(\beta/2+\alpha/2) \\ \cos(\theta/2)\sin(\beta/2-\alpha/2) \end{pmatrix}$$

with

$$|\vec{\boldsymbol{q}}_\Delta| = \sqrt{\sin^2\left(\frac{\theta}{2}\right)\sin^2\left(\frac{\beta+\alpha}{2}\right) + \sin^2\left(\frac{\theta}{2}\right)\cos^2\left(\frac{\beta+\alpha}{2}\right) + \cos^2\left(\frac{\theta}{2}\right)\sin^2\left(\frac{\beta-\alpha}{2}\right)}.$$

After parameterizing rotations along this geodesic with an angle φ the orientations of the geodesic sequence are given by

$$\boldsymbol{q}_{P_{\alpha,\beta,\varphi}} = \begin{pmatrix} \sin(\varphi/2)\vec{\boldsymbol{e}}_\Delta \\ \cos(\varphi/2) \end{pmatrix} \otimes \boldsymbol{q}_{P_1(\alpha)}$$

and thus

$$\boldsymbol{q}_{P_{\alpha,\beta,\varphi}} = \begin{pmatrix} -\frac{1}{|\vec{\boldsymbol{q}}_\Delta|}\sin\left(\frac{\varphi}{2}\right)\sin\left(\frac{\theta}{2}\right)\sin\left(\frac{\beta}{2}\right) \\ \frac{1}{|\vec{\boldsymbol{q}}_\Delta|}\sin\left(\frac{\varphi}{2}\right)\sin\left(\frac{\theta}{2}\right)\cos\left(\frac{\beta}{2}\right) \\ \sin\left(\frac{\alpha}{2}\right)\cos\left(\frac{\varphi}{2}\right) + \frac{1}{|\vec{\boldsymbol{q}}_\Delta|}\cos\left(\frac{\alpha}{2}\right)\sin\left(\frac{\varphi}{2}\right)\cos\left(\frac{\theta}{2}\right)\sin\left(\frac{\beta_j}{2}-\frac{\alpha_i}{2}\right) \\ \cos\left(\frac{\alpha}{2}\right)\cos\left(\frac{\varphi}{2}\right) - \frac{1}{|\vec{\boldsymbol{q}}_\Delta|}\sin\left(\frac{\alpha}{2}\right)\sin\left(\frac{\varphi}{2}\right)\cos\left(\frac{\theta}{2}\right)\sin\left(\frac{\beta_j}{2}-\frac{\alpha_i}{2}\right) \end{pmatrix}.$$

In the special case $\theta = 180^\circ \Rightarrow |\vec{\boldsymbol{q}}_\Delta| = 1$, and

$$\boldsymbol{q}_{P_{\alpha,\beta,\varphi}}|_{\theta=180^\circ} = \sin\left(\frac{\varphi}{2}\right)\begin{pmatrix} -\sin\left(\frac{\beta}{2}\right) \\ \cos\left(\frac{\beta}{2}\right) \\ \sin(\alpha/2)/\tan(\varphi/2) \\ \cos(\alpha/2)/\tan(\varphi/2) \end{pmatrix}. \quad (1)$$

As can be seen from Eq. (1), in this case the orientations $\boldsymbol{q}_{P_{\alpha,\beta,\varphi}}$ cover the complete orientation space and thus every possible diffraction pattern can be assigned to the sequences $P_{\alpha,\beta,\varphi}$. A proof using the Rodrigues formalism can be found in Appendix A.

IV. GIPRAL: A RECIPE IN TEN STEPS

This description motivates a new algorithm for orientation recovery, the geodesic and in-plane rotation algorithm (GIPRAL). It can be outlined as follows:

(1) Calculate diffraction pattern cross correlations $\tilde{C}(P_i,P_j)$ between all pairs (P_i,P_j) of diffraction patterns. Normalize and invert to obtain a dissimilarity measure as follows:

$$\tilde{d}_{\text{diss}}(P_i,P_j) = 1 - \tilde{C}(P_i,P_j)/\max_{k,l}\tilde{C}(P_k,P_l).$$

(2) Threshold nearest neighbors:

$$d_{\text{diss}}(P_i,P_j) = \begin{cases} \tilde{d}_{\text{diss}}(P_i,P_j) : \tilde{d}_{\text{diss}}(P_i,P_j) < \varepsilon \\ \infty \quad : \text{otherwise} \end{cases}.$$

(3) Select the initial diffraction pattern P_1, randomly or by visual inspection to guarantee that the desired object is chosen (as opposed to a blank shot or a shot containing artifacts as described in Refs. [9,12] like solvent droplets or clusters of the specimen object).

(4) Use Dijkstra's algorithm [11] to find the sequences with minimum accumulated dissimilarity from P_1 to every other diffraction pattern that is connected to P_1 (directly or indirectly). The threshold ε should be chosen to be high enough so all diffraction patterns are indirectly connected to P_1 and low enough so only very similar diffraction patterns are directly connected to P_1. In order to remove in-plane components from the sequence, add in-plane rotated copies $P_1(\alpha_i)$ of P_1 to the pool of diffraction patterns and set their dissimilarities $d_{\text{diss}}(P_1,P_1(\alpha_i))$ to zero before running Dijkstra's algorithm.

(5) Identify the end pattern P_2 as the one that maximizes $d_{\text{geo}}(P_1,P_2)$; it is the antipode to P_1 on $S(3)$, the three-sphere representing the orientations of SO(3). Because in-plane components have been suppressed in the previous step P_1 and P_2 are related by a true out-of-plane rotation.

(6) In case of object symmetries, start again, this time choose the previous P_2 as the new P_1. This avoids premature termination of the geodesic sequence due to symmetry (see Appendix C).

(7) Generate in-plane rotated diffraction patterns $P_1(\alpha_i)$ of P_1 and $P_2(\beta_j)$ of P_2 and keep track of their in-plane angles α_i and β_j. Put them into the pool of diffraction patterns and repeat step 1 and 2. At this stage it is not necessary to calculate every correlation anew; $d_{\text{diss}}(P_i,P_j)$ has to be updated only for the new diffraction patterns.

(8) Similarly to step 4 but without in-plane component suppression: Find geodesic sequences between all pairs $(P_1(\alpha_i),P_2(\beta_j))$.

(9) Determine the angle $\varphi_{i,j,k}$ between $P_1(\alpha_i)$ and the k^{th} diffraction pattern $P_{i,j,k}$ in the geodesic sequence between $P_1(\alpha_i)$ and $P_2(\beta_j)$ by interpreting the dissimilarity value between P_1 and P_2 as a single axis rotation of 180° (adapt in case of object symmetries).

(10) Relate the different rotation axes of different geodesics to each other using the known in-plane angles and $\varphi_{i,j,k}$.

The quaternion corresponding to the orientation of diffraction pattern $P_{i,j,k}$ with respect to P_1 is given by Eq. (1).

V. COMPUTATIONAL COMPLEXITY

The computational bottleneck of GIPRAL is the computation of pairwise dissimilarities between all pairs of diffraction patterns with a computational complexity of $\mathcal{O}(N^2)$ for N diffraction patterns. This can be sped up by parallelization, since the individual pairs are independent of each other. Moreover, the threshold ε sparsifies the dissimilarity matrix that is needed. If we assume that the triangle inequality holds for our estimate of d_{diss}, then we can update a table of upper and lower bounds for d_{diss} iteratively while adding entries to the dissimilarity matrix. These bounds can guide the computation of the next matrix elements, since elements with a lower bound $>\varepsilon$ can be rejected while elements with a small upper bound will be preferred. This way, only a fraction of all pairs of diffraction patterns needs to be taken into account.

VI. GENERALIZATION TO SYMMETRIC OBJECTS

Object symmetries complicate matters since symmetry operators can be applied to any orientation without altering the diffraction pattern dissimilarity. This leads to shortcuts on geodesic paths that act as "wormholes" in orientation space. A portion of the orientation space that consists of symmetrically irreducible orientations and therefore does not contain any "wormholes" can be constructed by applying symmetry operators to map every orientation to a symmetrically equivalent orientation such that the angular distance to a given reference orientation is minimized. These "fundamental zones" take very convenient shapes when expressed in Rodrigues-Frank (RF) parametrization [13]: For finite symmetry groups they are polytopes with planar boundaries. Moreover, geodesic paths are straight lines in RF space [13] (see Appendix A and Supplemental Material Fig. S1 [14] for an illustration), which makes RF space a natural choice for the formal treatment of rotational geodesics. The maximum angular separation that is possible under a given symmetry can be calculated from the shapes of all finite symmetry group classes [15]. These angles (see Ref. [16] for a complete list) correspond to the longest Euclidean distances between corners of the fundamental zone and can be used to relate geodesic paths of maximum length to angles in the case of symmetric objects. In Appendix B, we show how this can be used to navigate in the orientation space of symmetric objects and we discuss the coverage of the fundamental zone. Thus, GIPRAL can be used to recover the 3D diffraction volume using an ensemble of 2D diffraction snapshots irrespective of the underlying object symmetry.

VII. COMPARISON WITH OTHER APPROACHES

The geodesic distance is a combination of local distances between many data points into a conformable global distance, a principle which makes the isomap [17] algorithm so powerful and robust against outliers and noise. Fast dynamic programming approaches like Dijkstra's shortest path algorithm [11] are very efficient and guarantee globally optimal solutions. In-plane angles can be obtained with an accuracy that is only limited by the discrete nature of the pixel-based diffraction detection. Our GIPRAL method combines two reliable sources of angular information (in-plane, out-of-plane) without propagating the error exponentially by nesting steps which is treated by additional averaging in common-line or -arc methods [18,19]. Moreover, every pixel of the whole diffraction pattern contributes to the angular information. Orientation classification schemes proposed in Refs. [20,21] make use of the Pearson correlation coefficient to estimate the diffraction pattern similarity while [10] uses the Euclidean distance measure. We prefer the Pearson correlation coefficient because of its invariance under linear transformations of the diffraction intensities. As with Bayesian methods [22–24] the ensemble information of all diffraction patterns combined is used to infer object orientations, making GIPRAL also useful for data with very low photon counts [22,25]. Unlike the expectation maximization algorithms used in these methods, the dynamic programming algorithms applied in the geodesic search ensure that the global optimum is found. Compared to the graph-theoretic analysis of scattering data [10], GIPRAL refines simple pairwise local distances into an accurate integral distance measure and uses in-plane angles as an additional source of information. This reduces the orientation recovery to one-dimensional subproblems, making GIPRAL fast and physically intuitive.

VIII. APPLICATION OF GIPRAL TO EXPERIMENTAL DATA

So far, the efficacy of the published classification algorithms [10,18,22–24,26] for real data is largely unknown, whereas we here demonstrate successful application of GIPRAL to experimental XFEL snapshots. In order to test GIPRAL with real experimental data of a well-characterized model system we investigated aerosolized "nanorice," ellipsoidal iron-oxide nanoparticles. This system was studied previously [27] at the free electron laser in Hamburg (FLASH) but the data quality prevented a 3D reconstruction. Here we analyze 1000 diffraction patterns collected recently with 1.2-keV photons at the LCLS [9] of an inhomogeneous nanorice sample (see the transmission electron micrograph Fig. 4). The diffraction data has been deposited at CXIDB.org [28]. A random diffraction pattern P_1 was chosen, and following the procedure outlined in the above section, 128 diffraction patterns were aligned [Fig. 4(a)]. Higher-angle scattering is observed in the assembled 3D diffraction volume [Fig. 4(b)] than in individual patterns. On phase retrieval as described previously [29] we calculated the 3D reconstruction shown in Fig. 4(c). Shape, connectedness (smoothness), and size of the 3D electron density is consistent with both the diffraction volume and TEM measurements. The width and length of the reconstruction correspond to 8 and 30 voxels, respectively, with a voxel size of 5 nm. The injected nanorice sample does not have a homogeneous size distribution [Fig. 4(c)]. Indeed, not all collected diffraction patterns could be assigned to a common orientational alignment group. Picking one of the unassigned patterns as P_1', we applied the GIPRAL method to the remainder of the diffraction patterns and identified and aligned 52 patterns belonging to a subspecies of smaller particles (see the Supplemental Figure S2 [14]), in line with the size distribution

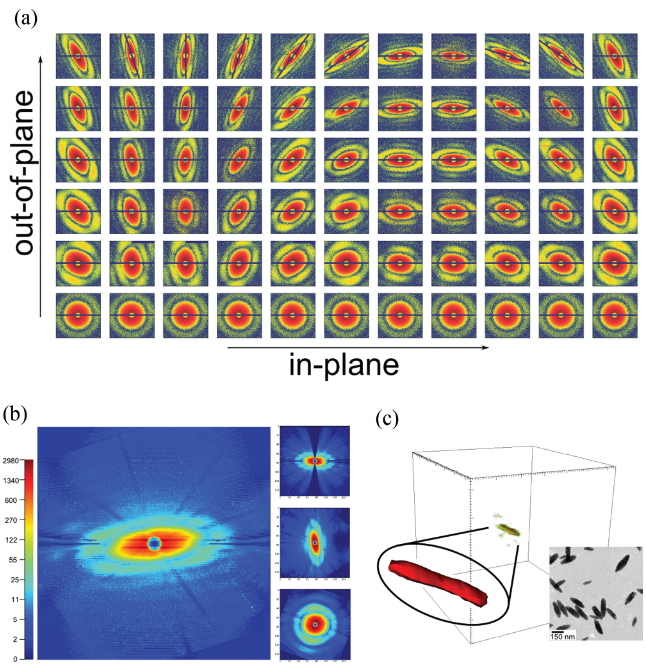

FIG. 4. (Color online) Application of the GIPRAL method to experimental XFEL snapshot diffraction data of an ironoxide nanoparticle, dubbed nanorice (a) GIPRAL output: orientation map of a subset of diffraction images collected at LCLS. Horizontal: in-plane; Vertical: geodesic out-of-plane rotations. (b) Slices through the 3D diffraction volume, assembled from the oriented 2D diffraction patterns. The color bar shows the the intensities in arbitrary digital units. (c) Reconstructed 3D electron density of a medium-sized 150-nm-long nanorice particle of the distribution shown in the TEM micrograph (inset). The bounding box depicts the oversampling volume. The magnified (red) object shows an isosurface representation.

of the sample established by transmission electron microscopy [Fig. 4(c), inset]. The separation of different subspecies is possible because only diffraction patterns that fit into the geodesics that are spanned between P_1 and P_2 are considered. In the case when two particles from different subspecies have similar diffraction patterns for specific orientations, a pattern from the "wrong" particle might be inserted into the diffraction volume, but since it fits in, it does not distort the volume.

In conclusion, we have introduced GIPRAL for orientation recovery of diffraction patterns and have demonstrated that it can be used to sort and orientationally align continuous diffraction patterns collected from an inhomogeneous ensemble of nanoparticles intersected by XFEL pulses in random orientations. This capability is of great relevance not only for the emerging single particle imaging of biological materials using FEL snapshots but also applicable for single particle cryoelectron microscopy, since large macromolecular complexes in particular are often conformationally or chemically inhomogeneous.

ACKNOWLEDGMENTS

We are grateful to Thomas R. M. Barends, R. Bruce Doak, Duane Loh, Wolfgang Kabsch, Abbas Ourmazd, Robert L. Shoeman, and John C. H. Spence for stimulating discussions and to Chris Roome and Frank Koeck for expert help with the IT. We acknowledge support from the Max Planck Society and Human Frontiers Science Program for funding.

APPENDIX A: RODRIGUES-FRANK SPACE

Geodesics of objects with rotational symmetries can be treated elegantly in the Rodrigues-Frank (RF) parametrization. RF parametrization is a mapping from SO(3) to $\mathbb{R}^3$. $\mathbb{R}^3$ is not a natural space for rotations, because it does not reflect the curvature of SO(3). In RF space, this problem is addressed by "flattening" out the round structure of rotations by mapping the rotations of 180° to infinity via a factor $\tan(\frac{\alpha}{2})$. The effect is that each circle representing a rotation has infinite curvature radius and is thereby flattened. RF space can be seen as a gnomonic projection of quaternions to Euclidean space. To the price of the nonlinear mapping of $\tan(\frac{\alpha}{2})$ comes a very nice property of RF space: The aforementioned flattening transforms geodesic lines into straight lines and the boundaries of Voronoi cells into planes. A rotation defined by a Euler axis $\hat{\boldsymbol{e}}$ and angle ϑ can be expressed as a RF vector $\boldsymbol{v} = \hat{\boldsymbol{e}} \tan(\frac{\vartheta}{2})$.

As shown in Ref. [13] a rotation $\boldsymbol{r}_1$ followed by a rotation $\boldsymbol{r}_2$ then takes the form

$$\boldsymbol{r}_1 \circ \boldsymbol{r}_2 = \frac{\boldsymbol{r}_1 + \boldsymbol{r}_2 - \boldsymbol{r}_1 \times \boldsymbol{r}_2}{1 - \boldsymbol{r}_1 \cdot \boldsymbol{r}_2}. \tag{A1}$$

From the definition, it is clear that geodesic movements that start from the reference orientation (the origin in RF space) are straight lines in RF space, because they are rotations about a single, fixed axis. This fixed axis defines the direction of the RF vector and the angle modulates the length. From (A1) it can be seen that geodesics are straight lines, even if the reference orientation is changed by applying a rotation to a new reference orientation first; see Ref. [15]. This means that all geodesic curves are straight lines in RF space.

The proof of full orientation coverage of Eq. (1) can be performed using the RF parametrization.

Since the orientation of P_1 is used as the reference orientation, its RF vector can be found at the origin $\mathrm{RF}(P_1) = (0,0,0)^T$ (this means that no rotation is necessary to reach the orientation of P_1 from the reference orientation). The in-plane rotations of P_1 are single-axis rotations and therefore geodesics, thus the points $\mathrm{RF}(P_1(\alpha))$ lie on a straight line $\boldsymbol{l}_1$ and the points $\mathrm{RF}(P_2(\beta))$ describe a straight line $\boldsymbol{l}_2$. The geodesics $P_{\alpha,\beta,\varphi}$ between $P_1(\alpha)$ and $P_2(\beta)$ then are the straight-line segments $\boldsymbol{l}_{\mathrm{geo}\alpha,\beta}$ that start at $\boldsymbol{l}_1$ and end at $\boldsymbol{l}_2$. Since we are free to choose any combination of α and β, every combination of start and end points on $\boldsymbol{l}_1$ and $\boldsymbol{l}_2$ is possible, and the possible geodesics $\boldsymbol{l}_{\mathrm{geo}}$ fill the convex hull of $\boldsymbol{l}_1$ and $\boldsymbol{l}_2$ (see Supplemental Material Fig. S1 [14] for an illustration).

The out-of-plane rotation axis $\vec{\boldsymbol{a}}$ is orthogonal to the x-ray axis $\vec{\boldsymbol{c}}$, therefore a parametric representation of $\boldsymbol{l}_2$ is $\boldsymbol{l}_2(t) = \frac{\tan(\theta/2)\vec{\boldsymbol{a}} + \tan(t\alpha/2)\vec{\boldsymbol{c}} - \vec{\boldsymbol{d}}(t)}{1}$, where $\vec{\boldsymbol{d}}(t) \sim \vec{\boldsymbol{a}} \times \vec{\boldsymbol{c}}$ is perpendicular to both $\vec{\boldsymbol{a}}$ and $\vec{\boldsymbol{c}}$. $\mathrm{RF}(P_2) = \tan(\theta/2) \cdot \vec{\boldsymbol{a}}$, so $\boldsymbol{l}_2(t) = \mathrm{RF}(P_2) + \vec{\boldsymbol{g}}(\mathrm{t})$, where $\vec{\boldsymbol{g}}(t)$ is orthogonal to $\mathrm{RF}(P_2)$, so the distance of $\boldsymbol{l}_2$ from the origin is $d = |\mathrm{RF}(P_2)| = \tan(\theta/2)$. $\boldsymbol{l}_1$ is parallel to $\vec{\boldsymbol{c}}$, so $\mathrm{RF}(P_2)$ is also orthogonal to $\boldsymbol{l}_1$ and since $\boldsymbol{l}_1$ contains the origin and $\boldsymbol{l}_2$ contains $\mathrm{RF}(P_2)$, d is the distance between $\boldsymbol{l}_1$ and $\boldsymbol{l}_2$ with $d \to \infty$ for $\theta \to 180°$.

As stated earlier, the convex hull of $\boldsymbol{l}_1$ and $\boldsymbol{l}_2$ contains all RF vectors that can be reached by a combination of out-of-plane geodesics and in-plane rotations. The boundaries of the convex hull of two infinite lines is given by two planes whose normals are orthogonal to both lines. The distance of these planes is the distance of the lines, and since $d \to \infty$, the half-space that is cut out of RF space by a plane that includes the origin is the space of all rotations reachable by patterns $P_{\alpha,\beta,\varphi}$. This half-space is sufficient to cover the full orientation space, since the other half represents equivalent rotations whose directions of the axes and the signs of the angles are inverted.

APPENDIX B: OBJECT SYMMETRIES IN RODRIGUES-FRANK SPACE

The geodesic analysis of GIPRAL is based on a diffraction pattern distance which is subject to the rotational specimen symmetry. Only the asymmetric unit can be explored, like wave vectors in a crystal that always reside in the first Brillouin zone. The analysis of in-plane rotations does not underlay this restriction, since the true angular distance measure can be used here. This has implications for the geodesic paths which GIPRAL identifies as shortest paths. The longest of these can only span half of the maximum angle which is irreducible under the object's symmetry. If additional diffraction patterns are added to the longest geodesic pattern sequence, there will be a different sequence that acts as a shortcut to the additional diffraction patterns to which they will then be attributed instead. In principle, there are ways to find longer geodesic sequences, but the notion of shortest paths is simple, robust, and efficient.

The fact that the "longest of all shortest" paths corresponds to a rotation of half the maximum possible object rotation subject to the symmetry can be used to calibrate the diffraction pattern based distance to an angular distance. Therefore, the maximum possible object rotation within the fundamental zone of the symmetry has to be known. This is similar to the maximum misorientation angle used in crystallographic texture analysis, for which RF space has proved to be an elegant tool [13,16].

The fundamental cells of all possible symmetry classes are listed in Ref. [16] and the maximum angle can be found as the longest RF vector within these cells, in the case of finite symmetry groups this is the RF vector of the cell vertices. Geometrically, it can be seen that the maximum angle is unique in the sense that it corresponds to rotation axes which are equivalent in terms of the symmetry operations. Thus, by identifying the "longest shortest paths," not only the angle but also the orientation of the rotation axis with respect to the symmetry axes of the specimen are determined. Due to the symmetry, there is a degeneracy of the maximum angle, since a rotation by an angle ω of the specimen around the maximal-angle-axis $\vec{\boldsymbol{d}}$ does not change the maximum geodesic distance. The axis $\vec{\boldsymbol{d}}$ restricts $\vec{\boldsymbol{c}}$ to the intersection $\boldsymbol{I}$ of the fundamental cell with a plane perpendicular to $\vec{\boldsymbol{d}}$ (because $\vec{\boldsymbol{c}} \perp \vec{\boldsymbol{d}}$). Within this plane the angle ω can be inferred with additional constraints: In-plane rotations are not restricted by the symmetry and thus the size of the fundamental cell in the direction of the in-plane rotations

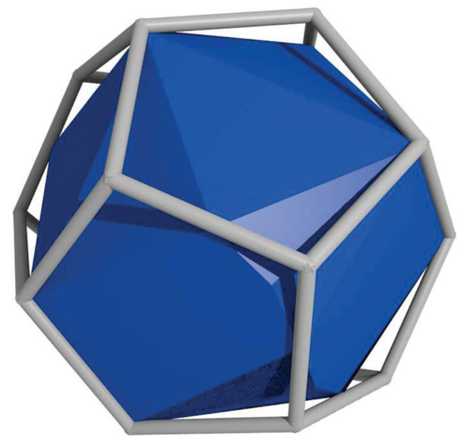

FIG. 5. (Color online) Fundamental cell in Rodrigues space for icosahedral symmetry (dodecahedron). The solid part can be reached by a combination out-of-plane geodesics and in-plane rotations of P_1 and P_2 in one go. Further iterations can then fill the whole fundamental cell. Due to the nonlinear deformation of Rodrigues space the gaps at the corner of the fundamental cell correspond to very small angular regions. In fact, the blue region corresponds to 92% of all possible orientations.

can be determined. The in-plane axis $\vec{\boldsymbol{c}}$ lies within the planar region $\boldsymbol{I}$ and the point p_{border} where it touches the border of the fundamental cell reveals the orientation of $\vec{\boldsymbol{c}}$ within $\boldsymbol{I}$ and can be used to obtain ω. The geodesic distance will be modulated by in-plane rotations such that jumps occur when in-plane rotations push $\boldsymbol{q}_{P_1(\alpha)}$ (or $\boldsymbol{q}_{P_2(\beta)}$) over the boundaries of the fundamental cell. These jumps can be used to identify p_{border}. Therefore, the orientation of both $\vec{\boldsymbol{d}}$ and $\vec{\boldsymbol{c}}$ with respect to the fundamental cell can be obtained and the diffraction snapshot orientations can be related to the object's symmetry axes.

When geodesics are identified as shortest paths the corresponding out-of-plane angle is restricted to only half of the maximum possible object rotation. Therefore the completeness of orientation coverage depends on the symmetry. However, because in-plane angles are not affected by the symmetry, the effect is not that severe. In the case of the dihedral symmetry of the nanorice test case (see Sec. VIII), complete coverage can be achieved. As an example of higher symmetries, we numerically identified the possible coverage to be 92% for icosahedral symmetry (see Fig. 5). Icosahedral symmetry is very common in nature and is of high importance for biological samples such as viruses.

APPENDIX C: PROJECTIONS AND MIRROR SYMMETRY

Suppose the object under consideration is symmetric under a mirror operation $\boldsymbol{M}$ and the object orientation $\boldsymbol{O}$ is such that the x-ray axis coincides with the normal of the mirror plane. If we approximate the image formation process by a parallel projection $\boldsymbol{P}$ along the x-ray axis, it follows $\boldsymbol{P}p = \boldsymbol{P}\boldsymbol{M}p$ for every point p. Suppose $\boldsymbol{R}^+$ is a rotation whose axis of rotation lies within the mirror plane of $\boldsymbol{M}$ and $\boldsymbol{R}^- := \boldsymbol{R}^{+^{-1}}$ is the inverse rotation (see Fig. 6). Then $\boldsymbol{R}^+ p = \boldsymbol{R}^+\boldsymbol{M}\boldsymbol{M}p = \boldsymbol{M}\boldsymbol{R}^-\boldsymbol{M}p$ because mirroring inverts the rotation direction. It follows that $\boldsymbol{P}\boldsymbol{R}^+ p = \boldsymbol{P}\boldsymbol{M}\boldsymbol{R}^-\boldsymbol{M}p = \boldsymbol{P}\boldsymbol{R}^-\boldsymbol{M}p$. Applied

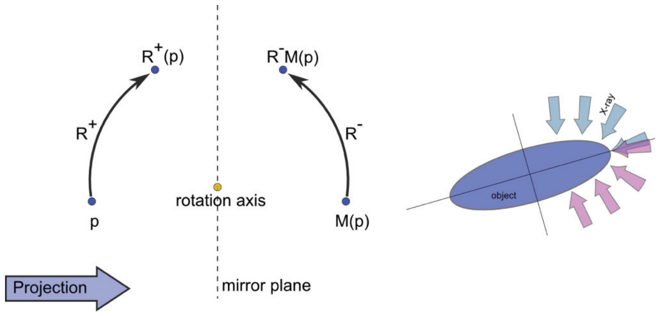

FIG. 6. (Color online) Mirror symmetry together with a projection operation leads to symmetry in rotation such that rotations in positive and negative direction yield the same projection. The diffraction pattern based geodesic sequence depicted by red arrows on the right side is equivalent to the blue sequence and it therefore stops at the mirror plane. It does not continue to the blue arrows as it would without symmetry.

to the set of object points, we can neglect the mirroring operation due to the symmetry $\Rightarrow \boldsymbol{P}\boldsymbol{R}^{+}p = \boldsymbol{P}\boldsymbol{R}^{-}p$. Thus, starting from the orientation $\boldsymbol{O}$, the sequence of diffraction patterns obtained by intermediates of the rotation $\boldsymbol{R}^{+}$ will be the same as for intermediates of its inverse, $\boldsymbol{R}^{-}$. Inversely, the sequence starting from $[\boldsymbol{O}, \boldsymbol{R}^{+}]$ going to $[\boldsymbol{O},\mathrm{Id}]$ gives a sequence of inverted element order compared to the sequence going from $[\boldsymbol{O},\mathrm{Id}]$ to $[\boldsymbol{O}, \boldsymbol{R}^{-}]$. Only a single rotation axis is involved and thus the full sequence from $[\boldsymbol{O}, \boldsymbol{R}^{+}]$ to $[\boldsymbol{O}, \boldsymbol{R}^{-}]$ is of geodesic nature. However, the diffraction pattern based distance will increase until $[\boldsymbol{O}, \mathrm{Id}]$ is reached and then decrease until it falls to zero when $[\boldsymbol{O}, \boldsymbol{R}^{-}]$ is reached. When we search for the maximum geodesic sequence starting from $[\boldsymbol{O}, \boldsymbol{R}^{+}]$, then $[\boldsymbol{O}, \mathrm{Id}]$ will be the end of the found sequence when only diffraction pattern based similarities are taken into account. This means that the geodesic sequences tend to end at mirror axes as shown in Fig. 6. This can be used to identify the symmetry of the object, as stated in Sec. III.

A stop at mirror axes means that geodesic sequences might become very short, depending on the the proximity of the start orientation of P_1 to mirror axes. But the sequence can be extended afterwards by making the orientation of the stop the new start orientation. The search for long geodesic sequences then yields sequences of maximal length.

APPENDIX D: ORTHOGONALIZING IN-PLANE AND OUT-OF-PLANE ROTATIONS

In the following considerations we will use a coordinate system that is fixed to the sample object. So instead of considering orientations of the sample we consider orientations of the x-ray beam and the detector. This implies that the in-plane axis changes from shot to shot. Three noncollinear points are sufficient to represent orientations. Since we do not consider translations, all orientations are related by rotation axes that have one point in common: the origin which is used as the first reference point r_0. r_0 is invariant for all shots. We choose the second reference point r_1 as the unit vector pointing along the x-ray beam and the third reference point r_2 is a point on the detector that does not coincide with the x-ray beam. The shortest (in an angular sense) rotation $\boldsymbol{R}_1$ that rotates r_1 of one shot to r_1' of a different shot is a rotation about an axis $\vec{\boldsymbol{e}}$ that is perpendicular to the x-ray beams of both shots: $\vec{\boldsymbol{e}} \perp \overline{r_0 r_1}$, $\vec{\boldsymbol{e}} \perp \overline{r_0 r_1'}$. After applying $\boldsymbol{R}_1$, the two reference points $\boldsymbol{R}_1 \cdot r_0 = r_0 = r_0'$ and $\boldsymbol{R}_1 \cdot r_1 = r_1'$ are aligned to the new orientation. To complete the rotation to the new orientation, also r_2 has to be rotated to r_2' by a rotation $\boldsymbol{R}_2$. $\boldsymbol{R}_2$ needs to leave r_0 and r_1' invariant, so its rotation axis is $\overline{r_0 r_1'}$ which is the new x-ray axis of the second shot, meaning $\boldsymbol{R}_2$ describes an in-plane rotation. Thus the complete relative rotation between the two shots is $\boldsymbol{R} = \boldsymbol{R}_2 \circ \boldsymbol{R}_1$. By construction no rotation that rotates r_1 to r_1' can be shorter than $\boldsymbol{R}_1$, meaning that the angle of the composition $\boldsymbol{R}$ is minimized when $\boldsymbol{R}_2 = \mathbb{1}$. Since $\boldsymbol{R}_2$ is an in-plane rotation, an in-plane-rotation of the second shot can be found such that upon replacing the shot with its in-plane rotation, $\boldsymbol{R} = \mathbb{1} \cdot \boldsymbol{R}_1$. Thus finding the shortest rotation between the two shots while allowing cost-free in-plane rotations of the second shot will yield a true out-of-plane rotation $\boldsymbol{R}_1$ with an axis that is orthogonal to the x-ray beam.

[1] J. Solem, JOSA B **3**, 1551 (1986).
[2] R. Neutze, R. Wouts, D. van der Spoel, E. Weckert, and J. Hajdu, Nature **406**, 752 (2000).
[3] H. N. Chapman *et al.*, Nature **470**, 73 (2011).
[4] S. Boutet *et al.*, Science **337**, 362 (2012).
[5] L. Redecke, K. Nass, D. P. DePonte, T. A. White, D. Rehders, A. Barty, F. Stellato, M. Liang, T. R. Barends, S. Boutet *et al.*, Science **339**, 227 (2013).
[6] M. Seibert *et al.*, Nature **470**, 78 (2011).
[7] D. Ne-Te Loh *et al.*, Nature **486**, 513 (2012).
[8] A. V. Martin *et al.*, Proc. SPIE **8078**, 807809 (2011).
[9] S. Kassemeyer *et al.*, Opt. Express **20**, 4149 (2012).
[10] D. Giannakis, P. Schwander, and A. Ourmazd, Opt. Express **20**, 12799 (2012).
[11] E. Dijkstra, Numer. Math. **1**, 269 (1959).
[12] C. H. Yoon, P. Schwander, C. Abergel, I. Andersson, J. Andreasson, A. Aquila, S. Bajt, M. Barthelmess, A. Barty, M. J. Bogan *et al.*, Opt. Express **19**, 16542 (2011).
[13] F. Frank, Metall. Trans. A **19**, 403 (1988).
[14] See the Supplemental Material at http://link.aps.org/supplemental/10.1103/PhysRevE.88.042710 for illustrations and additional results.
[15] A. Morawiec and D. Field, Philos. Mag. A **73**, 1113 (1996).
[16] A. Morawiec, J. Appl. Crystallogr. **28**, 289 (1995).
[17] J. Tenenbaum, V. De Silva, and J. Langford, Science **290**, 2319 (2000).
[18] V. Shneerson, A. Ourmazd, and D. Saldin, Acta Crystallogr. Sect. A **64**, 303 (2008).
[19] G. Bortel and M. Tegze, Acta Crystallogr. Sect. A **67**, 533 (2011).

[20] G. Huldt, A. Szőke, and J. Hajdu, J. Struct. Biol. **144**, 219 (2003).
[21] G. Bortel, G. Faigel, and M. Tegze, J. Struct. Biol. **166**, 226 (2009).
[22] R. Fung, V. Shneerson, D. Saldin, and A. Ourmazd, Nat. Phys. **5**, 64 (2008).
[23] D. Ne-Te Loh *et al.*, Phys. Rev. E **80**, 026705 (2009).
[24] B. Moths and A. Ourmazd, Acta Crystallogr. Sect. A **67**, 481 (2011).
[25] H. Philipp, K. Ayyer, M. Tate, V. Elser, and S. Gruner, Opt. Express **20**, 13129 (2012).
[26] A. Tokuhisa, J. Taka, H. Kono, and N. Go, Acta Crystallogr. Sect. A **68**, 366 (2012).
[27] N. D. Loh *et al.*, Phys. Rev. Lett. **104**, 225501 (2010).
[28] Filipe R N C Maia, Nat. Meth. **9**, 854 (2012).
[29] J. Steinbrener, Ph.D. thesis, University of New York at Stony Brook, 2010.